

Introducing Metal–Organic Frameworks to Melt Electrowriting: Multifunctional Scaffolds with Controlled Microarchitecture for Tissue Engineering Applications

Salma Mansi, Sarah V. Dummert, Geoffrey J. Topping, Mian Zahid Hussain, Carolin Rickert, Kilian M. A. Mueller, Tim Kratky, Martin Elsner, Angela Casini, Franz Schilling, Roland A. Fischer, Oliver Lieleg, and Petra Mela*

Scaffolds with multiple advantageous biological and structural properties are still a challenge in the field of tissue engineering. The convergence of advanced fabrication techniques and functional materials is key to fulfill this need. Melt electrowriting (MEW) is an additive manufacturing technique that enables the fabrication of microfibrillar scaffolds with precisely defined microarchitectures. Here, it is proposed to exploit metal–organic frameworks (MOFs) to efficiently introduce multifunctionalities by combining polycaprolactone (PCL), the gold standard material in MEW, with a silver-/silver-chloride-decorated iron-based MOF (NH₂-MIL-88B(Fe)). This results in highly ordered constructs with antibacterial properties and magnetic resonance imaging (MRI) visibility. Scaffolds with up to 20 wt% MOF are successfully melt-electrowritten with a fiber diameter of 50 μm. Among these, 5 wt% MOF proves to be the optimal concentration as it exhibits silver-induced sustained antibacterial efficacy while maintaining PCL cytocompatibility and in vitro immune response. The iron component of the MOF (Fe(III) nodes) renders the composite visible with MRI, thereby enabling scaffold monitoring upon implantation with a clinically accepted method. The combination of MEW and MOFs as tunable additives and cargo carriers opens the way for designing advanced multifunctional scaffolds with a wide range of applications in, e.g., tissue engineering, biosensing and drug delivery.

1. Introduction

Scaffolds for tissue engineering applications need to meet a variety of requirements, from a defined structural and mechanical microenvironment to material properties that enable an optimal interaction with the host.^[1] Manufacturing microfibrillar scaffolds with controlled microarchitecture and application-specific properties is a major goal in the field of tissue engineering that calls for the convergence of advanced fabrication methods and innovative materials.


Melt electrowriting (MEW) is an additive manufacturing technique that is uniquely capable of producing polymeric scaffolds with precise microarchitecture. Molten polymers are extruded into microfibers and deposited on a collector according to a precoded pattern by exploiting the electrohydrodynamic fiber formation process.^[2–5] MEW has shown promising results in tissue engineering of bone, cartilage, skin, and cardiovascular structures.^[6–11] While

S. Mansi, K. M. A. Mueller, P. Mela
Medical Materials and Implants
Department of Mechanical Engineering
Munich Institute of Biomedical Engineering and TUM School of
Engineering and Design
Technical University of Munich
Boltzmannstraße 15, 85748 Garching, Germany
E-mail: petra.mela@tum.de

S. V. Dummert, M. Z. Hussain, R. A. Fischer
Inorganic and Metal-Organic Chemistry
Department of Chemistry
TUM School of Natural Sciences
Technical University of Munich
Lichtenbergstraße 4, 85748 Garching, Germany

G. J. Topping, F. Schilling
Department of Nuclear Medicine
School of Medicine
Klinikum rechts der Isar
Technical University of Munich
Ismaninger Straße 22, 81675 Munich, Germany

C. Rickert, O. Lieleg
Biomechanics
Department of Materials Engineering
TUM School of Engineering and Design
Technical University of Munich
Ernst-Otto-Fischer Straße 8, 85748 Garching, Germany

 The ORCID identification number(s) for the author(s) of this article can be found under <https://doi.org/10.1002/adfm.202304907>

© 2023 The Authors. Advanced Functional Materials published by Wiley-VCH GmbH. This is an open access article under the terms of the Creative Commons Attribution-NonCommercial License, which permits use, distribution and reproduction in any medium, provided the original work is properly cited and is not used for commercial purposes.

DOI: 10.1002/adfm.202304907

the application range is increasingly being expanded, MEW could significantly profit from the development of new materials. Indeed, the library of polymers that have been processed so far is still limited, with polycaprolactone (PCL) serving as the gold standard.^[12] The need for scaffolds with tailored biological and mechanical properties has resulted in the use of composites, where additives are combined with the polymer to be printed. For instance, Kade et al. incorporated carbonyl iron particles in poly(vinylidene fluoride) (PVDF) to melt electrowrite scaffolds for application in magnetoactive cell stimulation.^[13] Somszor et al. used PCL and graphene oxide to manufacture stents with thin struts and improved mechanical strength.^[14] Mueller et al. achieved magnetic resonance imaging (MRI) visibility of melt-electrowritten PCL scaffolds with embedded ultrasmall super-paramagnetic iron oxide (USPIO) particles.^[15] Although these and similar approaches have shown great potential for adding new properties to melt-electrowritten constructs, they typically introduce only one functionality.^[15–22,8]

In this study, we converge MEW, as advanced fabrication technique, with metal–organic frameworks (MOFs), a class of promising yet underexploited materials, to obtain multifunctional scaffolds. MOFs are solid-state coordination polymers that consist of metal nodes, either ions or clusters, connected by multitopic organic linkers resulting in porous, open framework structures.^[23,24] MOFs can be based on multiple metal ions, where the second metal ion can either be incorporated as a metal ion to the framework, coordinated to the linker, or hosted in the cavities (by loading/impregnation). Therefore, MOFs are capable of serving multiple applications.^[25–27] Furthermore, the organic linkers of MOFs could be either partially or fully exchanged for other linkers or be modified with different functional groups, such as amino moieties, to add new properties to the compounds. Additionally, the available pores of the MOFs (present at the internal or external MOF crystallite surface) can be loaded with different cargos, e.g., nanoparticles, gases, and drug molecules. Loading a cargo into the MOF pores and its controlled release have been successfully applied to gas storage and catalysis. However, only recently, interest in using MOFs for biomedical applications has grown, e.g., for drug delivery, antibacterial effect, biosensing, and bioimaging.^[28–42] So far, most approaches tested the MOF powders as prepared and applications mainly focused on surface

coatings.^[43–46] Only few studies looked into embedding MOFs into scaffolds for tissue engineering, all of them using electrospinning as fabrication technique.^[47–49] However, besides lacking the capability for precise microarchitectures unique to MEW, these approaches used MOFs to introduce only one additional property, leaving their vast potential toward multifunctional scaffolds largely unexploited.

With the ultimate aim of establishing a platform for multifunctional scaffolds with application-specific properties, we start by selecting an iron-based and silver-decorated MOF as candidate to confer antibacterial properties and concurrent MRI visibility to MEW constructs. The use of silver species as an antibacterial agent^[50–52] mitigates the problem of multidrug resistant strains created through the excessive use of antibiotics. At the same time, the nontoxic iron nodes of the nanoscale MOF confer MRI visibility to PCL, which would be beneficial for the clinical translation of tissue engineering scaffolds to patients, as MRI shows optimal contrast resolution for soft tissues and would allow monitoring of the implant noninvasively. Furthermore, this iron-based MOF has been shown to be biocompatible in *in vivo* studies when delivered as a powder.^[53–55] To the best of our knowledge, this is the first study showing the potential of converging MEW and MOFs by fabricating PCL scaffolds featuring controlled microarchitecture and additional target functionalities. We thoroughly characterize the constructs morphologically, chemically, rheologically, biologically, and by MRI. This study paves the way for designing and manufacturing advanced multifunctional tissue engineering scaffolds by MEW.

2. Results and Discussion

The synthesis of NH₂-MIL-88B(Fe) (from now on referred to as MOF–Fe) and the immobilization of silver species onto the MOF–Fe according to modified literature protocols,^[56] were confirmed by powder X-ray diffraction (PXRD), Fourier-transform infrared spectroscopy (FTIR), thermogravimetric analysis (TGA), transmission electron microscopy (TEM), X-ray photoelectron spectroscopy (XPS), and Brunauer–Emmett–Teller (BET) measurements of the as-prepared powders (for full details and analytical data, see the Experimental Section). As shown in **Figure 1a**, characteristic reflections appearing at 2θ values of 9.2° (002) and 10.3° (101) in PXRD patterns match with the reported diffractogram of the Cambridge crystallographic data centre (CCDC: 647646) and thus confirm the phase pure synthesis of the MOF–Fe.^[57] After the loading of silver species onto the MOF–Fe, (from now on referred to as MOF–Fe/Ag) no shift in the main XRD peaks was observed, which indicates structural stability of the framework. However, some low intensity broad new reflections were observed at 2θ values of 27.8° , 32.2° , 38.2° , 44.2° , 46.2° , 54.8° , and 57.3° , which indicate the formation of two different species of silver nanoparticles (NPs).^[58,59] While two of these reflections (38.2° , 44.2°) can be assigned to elemental silver in face-centered cubic structure (Ag, CCDC: 1690325), the others correspond to the PXRD pattern of silver chloride (AgCl, CCDC: 1626914). The formation of AgCl alongside with elemental Ag during solution impregnation with AgNO₃ can be attributed to the composition of NH₂-MIL-88B, [Fe₃Cl(H₂O)₂O(NH₂–BDC)₃] as a consequence of the use of FeCl₃·6H₂O as the source of Fe^{2+/3+} ions (NH₂–BDC,

T. Kratky
Physical Chemistry with Focus on Catalysis
Department of Chemistry
TUM School of Natural Sciences
Technical University of Munich
Lichtenbergstraße 4, 85748 Garching, Germany
M. Elsner
Chair of Analytical Chemistry and Water Chemistry
School of Natural Sciences
Department of Chemistry
Technical University of Munich
Lichtenbergstrasse 4, 85748 Garching, Germany
A. Casini
Chair of Medicinal and Bioinorganic Chemistry
School of Natural Sciences
Department of Chemistry
Technical University of Munich
Lichtenbergstrasse 4, 85748 Garching, Germany

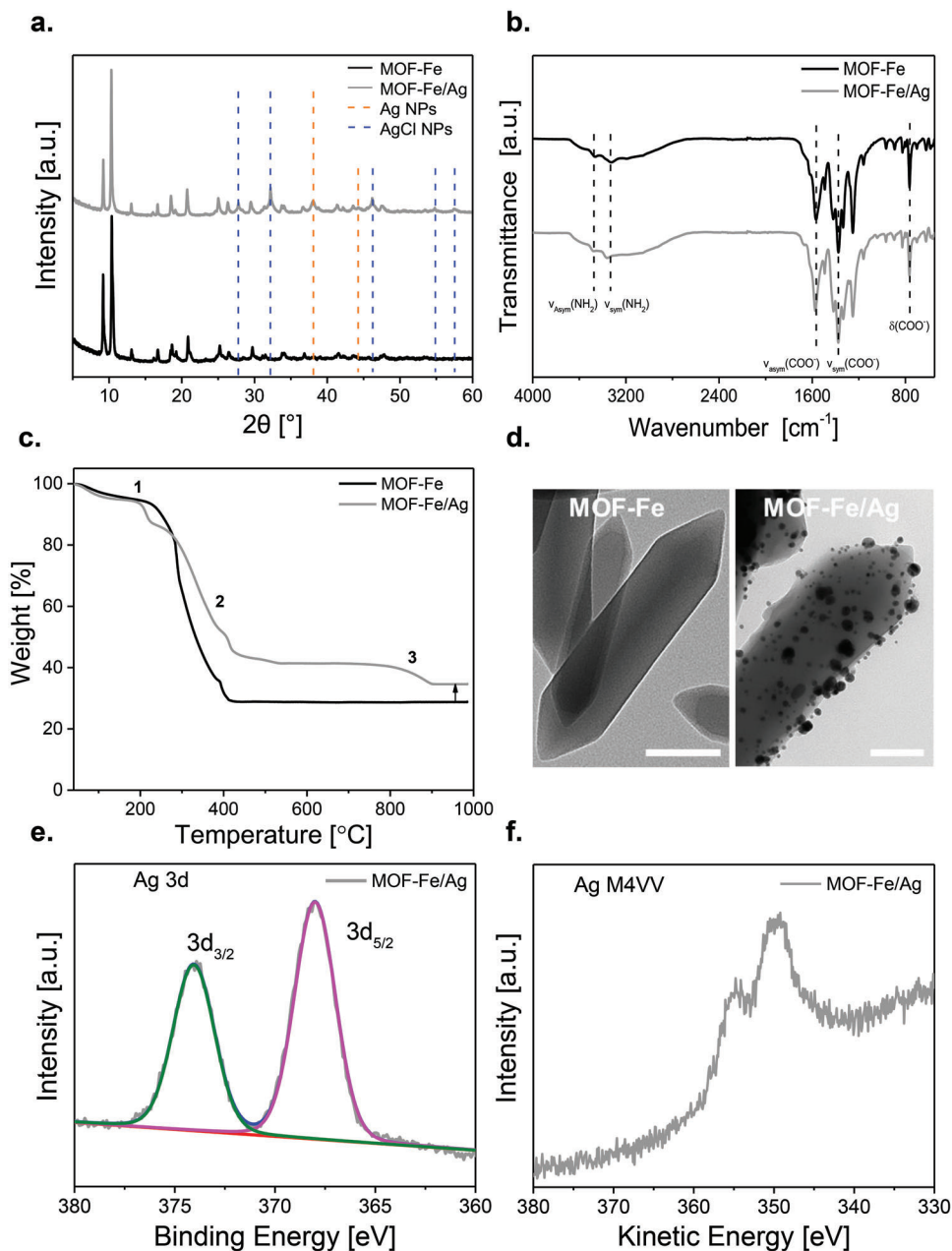


Figure 1. Characterization data of MOF–Fe and MOF–Fe/Ag. a) PXRD patterns, b) FTIR spectra, c) TGA curves, and d) TEM images of the as-synthesized MOF powders, MOF–Fe and MOF–Fe/Ag. Scale bar: 100 nm. The silver species in MOF–Fe are in the form of Ag/AgCl nanoparticles, decorated mostly on the outer surface of MOF–Fe. e) High resolution XPS spectra Ag 3d and f) Auger parameter spectrum of Ag M4VV in MOF–Fe/Ag.

BDC = 1,4-benzenedicarboxylate). The FTIR spectra (Figure 1b) of MOF–Fe and MOF–Fe/Ag exhibited similar vibrational modes. The vibrational bands observed at 1567, 1373, and 765 cm^{-1} are assigned to $\nu_{\text{Asym}}(\text{COO}^-)$, $\nu_{\text{sym}}(\text{COO}^-)$, and $\delta(\text{COO}^-)$, respectively, for the coordinated carboxylate (organic linker) groups to the iron nodes. In the FTIR spectra of MOF–Fe and MOF–Fe/Ag, no apparent shift was observed in the abovementioned vibrational modes, suggesting that the incorporation of Ag(I) does not replace the framework Fe(III), resultantly, the chemical coordination environments of the iron metal nodes and the carboxylic groups of the organic linker remain unchanged.

The relative amount (wt%) of iron and silver was calculated from the weight loss observed in the TGA curves of pristine MOF–Fe and MOF–Fe/Ag powders at 1000 °C under synthetic air. As shown in Figure 1c, a small weight loss (labeled as 1) at lower temperature (below 250 °C) was due to the release of adsorbed moisture and the residual solvent. The major weight loss (labeled as 2) observed between 250 and 550 °C, is due to the dissociation of the organic linker and metal nodes, resulting in the formation and release of NO_x and CO_x . In the sample MOF–Fe/Ag, another weight loss (labeled as 3) was observed between 800 and 900 °C suggesting the thermal reduction of AgCl,

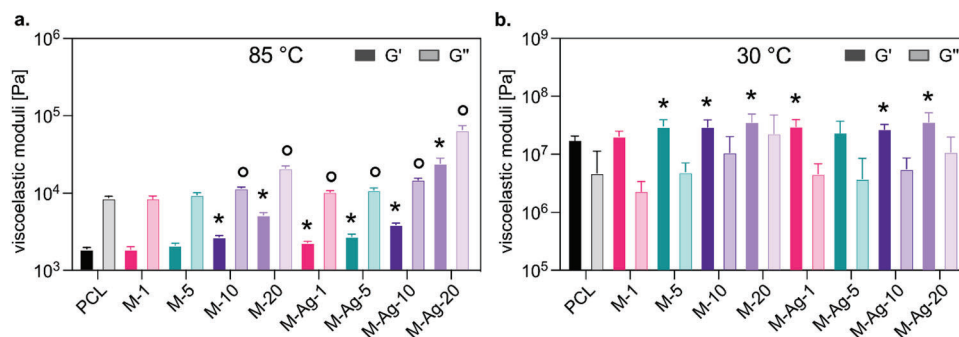


Figure 2. Storage and loss modulus of PCL and PCL with embedded MOF–Fe or MOF–Fe/Ag (denoted as M-1, M-5, M-10, or M-20, and M–Ag-1, M–Ag-5, M–Ag-10, or M–Ag-20), at a) 85 °C and b) 30 °C at a frequency of 1 Hz. Values represent mean \pm standard deviation as obtained from $n = 5$ independent samples. Different colors represent different MOF concentrations. Asterisks and circles denote statistically significant differences to the storage modulus (G') and the loss modulus (G'') of PCL (measured at the same temperature), respectively.

which subsequently will form Ag(0) (confirmed by PXRD, Figure S5, Supporting Information). The residual samples were collected after TGA, and their XRD patterns were recorded (Figure S5, Supporting Information) to find out their crystalline structures. As expected, the thermal decomposition of MOF–Fe/Ag under synthetic air (heated up to 1000 °C) resulted in Fe₂O₃ and Ag(0). The relative amounts of iron and silver metals were calculated to be 19.2% and 5.8%, respectively. This relative composition correlates to the amount of iron and silver present in pristine MOF–Fe/Ag. The results are also summarized in Table S1 (Supporting Information).

The MOF-supported silver species were further characterized by (TEM) to observe the distribution of Ag species over MOF–Fe. As shown in Figure 1d (right), Ag/AgCl NPs are uniformly distributed over spindle-shaped MOF–Fe crystals. Using the MOF as a support not only allows for a homogeneous distribution of the NPs throughout the system but also helps to prevent their aggregation. For comparison, more TEM images of MOF–Fe and MOF–Fe/Ag are shown in Figure S6 (Supporting Information). The XPS of MOF–Fe/Ag was performed to further confirm the chemical nature of loaded Ag species. It is rather challenging to determine the oxidation state of Ag species because the Fe 2p core level (Figure S7, Supporting Information) overlaps with the Ag 3s core level. The fit did not allow for a deconvolution of both core levels. However, the Ag 3d (Figure 1e) fit revealed one component. The binding energy alone was not very helpful to address the oxidation state of Ag. Therefore, the Auger parameter using the Ag 3d_{5/2} and Ag M4VV signals (Figure 1f) was calculated. The obtained Auger parameter value of 723 eV is relatively lower as compared to metallic Ag(0), which hints that the Ag species are not purely in metallic form. Supported by PXRD results and TGA, it can be inferred that Ag species are predominantly present in the form of AgCl NPs, mostly decorated at the surface of MOF–Fe crystallites (also confirmed by high resolution TEM images) partially covering the Fe species, leading to attenuation.

The specific surface areas of desolvated MOF–Fe and MOF–Fe/Ag (Figure S8, Supporting Information) were measured to be 61 and 54 m² g^{−1}, respectively, in accordance with the literature. It should be noted that this comparably low surface area is due to poor accessibility of N₂ in the desolvated, closed-pore form, caused by the flexible (breathing) nature of the par-

ticular MOF–Fe framework.^[60,61] The small reduction in surface area of MOF–Fe/Ag can be attributed to the partial pore blocking by Ag/AgCl NPs. Since most of the loaded Ag/AgCl are decorated at the external particle surface of MOF–Fe, the free pores (though closed in activated form due to breathing/gating behavior) in MOF–Fe/Ag make it very promising to be used as a customizable multifunctional drug delivery system.

The composite materials PCL/MOF–Fe or PCL/MOF–Fe/Ag were fabricated by suspending the MOF powder in a chloroform solution of PCL, as described in the Experimental Section. The viscoelastic behavior of PCL with embedded MOF–Fe or MOF–Fe/Ag was determined at 85 and 30 °C, which represents the needle temperature and the collector temperature of the MEW setup, respectively. The PCL/MOF composite material samples prepared with 1, 5, 10, and 20 wt% of MOF–Fe and MOF–Fe/Ag in PCL are referred to as M-1, M-5, M-10, and M-20, and M–Ag-1, M–Ag-5, M–Ag-10, or M–Ag-20, respectively. At 85 °C, pure PCL showed characteristics that are typical for a viscoelastic fluid (Figure 2a), with the loss modulus G'' dominating over the storage modulus G' for all tested frequencies as determined from frequency sweeps (Figure S11, Supporting Information). This behavior was not changed by adding either MOF–Fe or MOF–Fe/Ag, whereby the moduli slightly increased with respect to those of pure PCL (Figure 2a). At 30 °C the samples were dominated by elastic properties (Figure 2b). With those results in mind, we expected that the MOF loading into PCL did not preclude printability of the composites.

Indeed, we were able to melt electrowrite all prepared composites and to identify suitable parameters to obtain a steady process that would result in fibers with the same diameter and a smooth surface. Precise MEW of the different PCL/MOF–Fe/Ag composites with MOF–Fe/Ag contents as high as 20% was achieved, as demonstrated by the well-ordered grid structure in Figure 3a–f. Increasing amounts of MOF–Fe/Ag produced a visible color change of the scaffolds from near white to dark brown (Figure 3a). The results of the printing parameter optimization summarized in Table 1 showed that the applied pressure was increased from 2 to 3 bar for scaffolds with embedded MOF–Fe/Ag. The voltage varied between 4.4 and 5.4 kV and the translation speed between 325 and 540 mm min^{−1}. The larger fiber diameter of the PCL/MOF–Fe/Ag composites (Figure 3g) was a result of the increase in applied pressure and

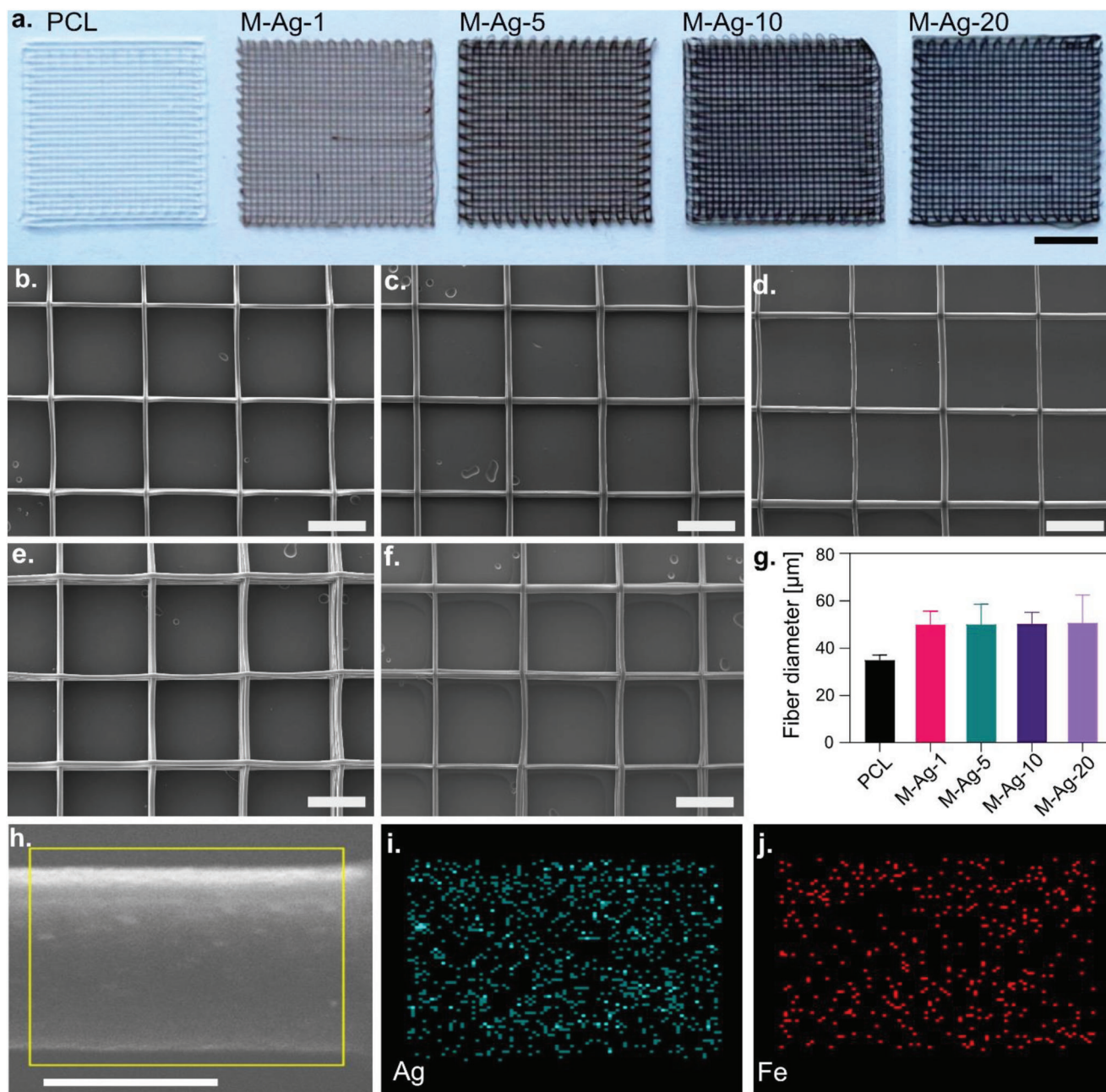


Figure 3. Images of melt-electrowritten PCL and PCL/MOF-Fe/Ag constructs (denoted as M-Ag-1, M-Ag-5, M-Ag-10, or M-Ag-20). a) Macroscopic images of melt-electrowritten PCL scaffolds with increasing percentage of MOF-Fe/Ag. Scale bar: 10 mm. SEM images of the scaffolds: b) PCL, c) M-Ag-1, d) M-Ag-5, e) M-Ag-10, f) M-Ag-20. Scale bar: 500 μm. g) Fiber diameter as function of the MOF-Fe/Ag weight percentage. Values represent mean ± standard deviation obtained from 20 measurements from a total of $n = 3$ independent samples. h) SEM image of an M-Ag-5 fiber and its i) silver and j) iron distribution by EDX elemental mapping. Scale bar: 20 μm.

voltage and of the lower translation speed. The particles embedded in PCL likely interfere with the electric forces pulling the polymer jet toward the collector, thereby resulting in higher voltages and lower speeds being necessary to precisely deposit the fibers on the collector. The chemical and structural stability of the MOF-Fe/Ag after MEW was verified by grazing incidence X-ray diffraction (Figure S9, Supporting Information), while the thermal stability was confirmed by TGA and dif-

ferential scanning calorimetry (DSC) (Figure S10, Supporting Information).

The energy dispersive X-ray spectrometry (EDX) elemental mapping of a PCL/MOF-Fe/Ag sample (M-Ag-5) shows the homogeneous distribution of Fe and Ag in the fiber (Figure 3h-j). We estimate a penetration depth of X-rays of ≈ 10 μm, taking into consideration the acceleration voltage of 20 kV and the relatively low density of PCL/MOF-Fe/Ag. The distribution

Table 1. MEW parameters of the composite scaffolds.

	Voltage [kV]	Pressure [bar]	Translation speed [mm min ⁻¹]
PCL	4.8	2	450
M–Ag-1	4.4	3	540
M–Ag-5	4.9	3	325
M–Ag-10	4.9	3	380
M–Ag-20	5.4	3	325

of the MOF within the fibers was qualitatively confirmed by scanning electron microscopy (SEM) imaging of the cross-section of MEW fibers broken in liquid nitrogen (Figure S14, Supporting Information). The presence of the MOF–Fe/Ag did not affect the interlayer bonding of the melt-electrowritten scaffolds as shown by tensile testing, performed according to a previous study,^[62] nor did the incubation of the scaffolds in phosphate buffered saline (PBS) (Figure S15, Supporting Information). This was qualitatively confirmed by the SEM images showing the fiber necking occurring during printing of stacked crossing and aligned fibers (Figure S16, Supporting Information). We also did not observe any effect of the MOF loading when printing scaffolds with higher layer numbers (data not shown).

The MEW of composites with a high particle content has been reported only in few studies.^[13,16] For instance, Kade et al. achieved the incorporation of carbonyl iron particles in PVDF at 15 wt% with homogeneous fibers, whereas 30% particle loading resulted in heterogenous fiber morphology. In our study, it was possible to melt electrowrite PCL/MOF–Fe/Ag composites with MOF–Fe/Ag contents up to 20 wt% resulting in well-ordered grid structures. Such a high MOF loading into the polymer matrix could be particularly attractive for drug delivery applications, for example, to achieve sustained therapeutically active drug levels.^[63–66]

As described above, the Ag species immobilized on the MOF consist of Ag (0) and AgCl NPs. In general, the antibacterial activity of Ag compounds can be ascribed to different pathways: a) the binding to and damage of the function of cell membranes and DNA; b) the release of silver ions that disrupt bacterial membranes, metabolic processes, DNA, and proteins in multiple ways, and c) the generation of reactive oxygen species (ROS), which are highly unstable molecules and can severely damage the DNA and the membrane, as well as disrupt a variety of metabolic processes.^[67] While studies to fathom the exact nature of these various modes of action are still ongoing, it is believed that physicochemical properties such as stability, size, shape, and surface chemistry of the silver species are of major importance. Furthermore, Ag and AgCl are both known to possess antibacterial activity, and it was shown that they generated similar amounts of ROS in *Escherichia coli*.^[68] In case of our melt-electrowritten PCL/MOF–Fe/Ag composites, we propose that the MOF–Fe/Ag acts as a “depository” of Ag/AgCl, where mobile Ag⁺ ions (from predominant AgCl) as well as Ag (elemental silver) are released from the NP-“depot” state to interact with the microbial cells. The antibacterial efficacy assessment of PCL/MOF–Fe/Ag scaffolds showed a reduction in bac-

terial colony forming units (CFUs) that became stronger with increasing MOF–Fe/Ag concentration (Figure 4). By contrast, no reduction in CFUs was observed for PCL scaffolds with embedded MOF–Fe sans loaded Ag/AgCl (Figure S12, Supporting Information), attributing the antibacterial activity to the Ag/AgCl NPs decorated on the MOF–Fe. Notably, the M–Ag-20 scaffolds had a 6-log reduction of the bacterial concentration for all three strains tested: *E. coli*, *Staphylococcus epidermidis*, and *Staphylococcus aureus* (Figure 4a–c). This underscores the broad-range antibacterial activity of Ag toward different pathogenic strains.^[69–76]

The melt-electrowritten scaffolds were tested for their cytocompatibility with an indirect test according to the international organization for standardization (ISO) 10993. At day 3, cells incubated with the eluates of MEW constructs with 10 and 20 wt% MOF–Fe/Ag embedded in PCL showed a cell viability below 70% and were, therefore, cytotoxic according to the ISO standard. Conversely, up to 5 wt% MOF–Fe/Ag embedded in PCL showed good cytocompatibility (Figure 5). PCL/MOF–Fe constructs were cytocompatible even at 20 wt% MOF (Figure 5 and Figure S13 (Supporting Information)), indicating that silver was responsible for the toxicity, in agreement with previous studies showing increasing toxicity on different cell lines with increasing pure silver content.^[50,72,74,77–81]

Importantly, PCL scaffolds loaded with only 5 wt% MOF–Fe/Ag already showed excellent antibacterial efficacy corresponding to an average log-reduction of 2.6, equivalent to 99.5% germ reduction, while being cytocompatible. Therefore, these scaffolds were considered as ideal for tissue engineering applications and were further investigated. For applications other than tissue engineering, PCL scaffolds with higher percentage of MOF–Fe/Ag would be advantageous and the self-sterilizing properties highly desirable, for example, for antibacterial microporous membranes for filtration applications. For the remainder of this study, however, PCL scaffolds with 10 and 20 wt% MOF–Fe/Ag were not further considered.

The antibacterial efficacy and cytocompatibility of the melt-electrowritten PCL over an eight-week incubation time in cell culture medium are shown in Figure 6a,b. The cell viability of the composite scaffolds is maintained after 8 weeks of incubation in cell culture medium. The antibacterial efficacy of the incubated MEW scaffolds presents an average of 2-log reduction over the entire incubation period, equivalent to an average germ reduction of 98.3%. These results stress the potential of the composite scaffolds for having a long-term sustained antibacterial effect and thereby potentially preventing biofilm formation on the scaffolds and lowering the risk of infection. This was further confirmed in an accelerated degradation study, during which M–Ag-5 samples were incubated in PBS at 50 °C for 12 days. Measurements of the PBS supernatant by inductively coupled plasma mass spectrometry (ICP-MS) at days 1, 6, and 12 show a stable release over the whole duration of the study (Figure S18, Supporting Information). Evaluation of the pH of the sample supernatants indicated no significant effect of the presence of the MOF on the pH during the degradation of PCL. Similar values were also observed for the weight with a moderate tendency toward lower values, although not always statistically significant. These results could be explained by the presence of the MOF particles as defects in

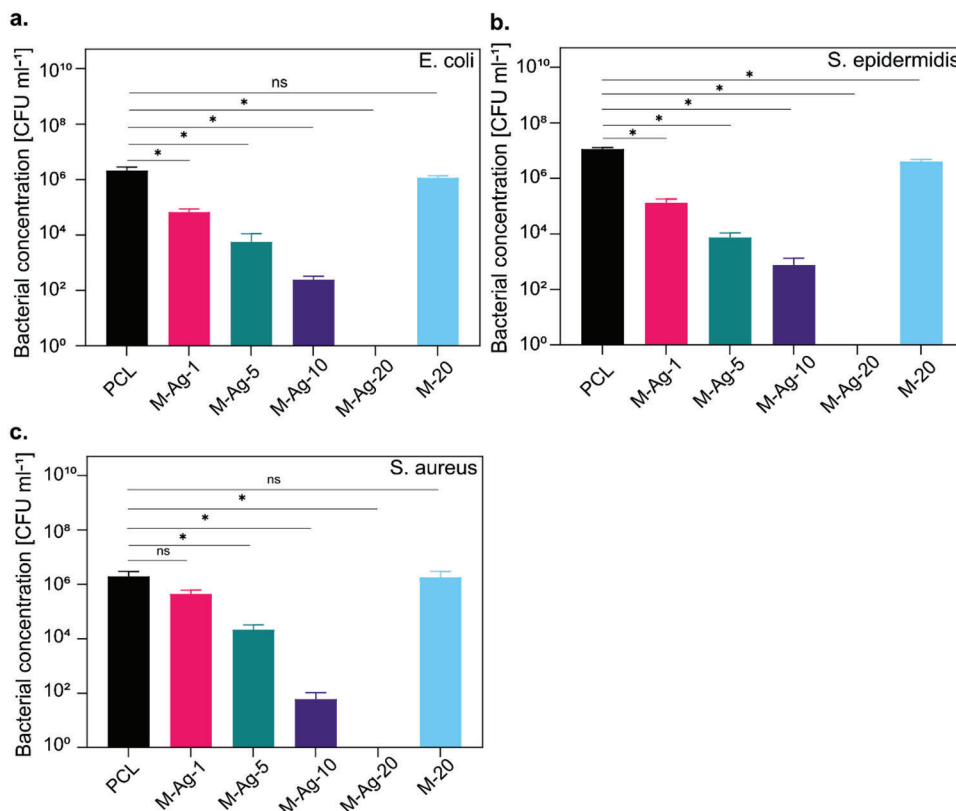


Figure 4. Overview of the antibacterial efficacy of the melt-electrowritten PCL, PCL/MOF–Fe/Ag, and PCL/MOF–Fe scaffolds. Bacterial concentration in colony forming units (CFUs) is determined on the melt-electrowritten scaffolds for a) *E. coli*, b) *S. epidermidis*, c) and *S. aureus*. Values represent mean \pm standard deviation as obtained from $n = 3$ independent samples.

the polymer matrix and their interaction with the phosphate^[82,83] (Figure S17, Supporting Information).

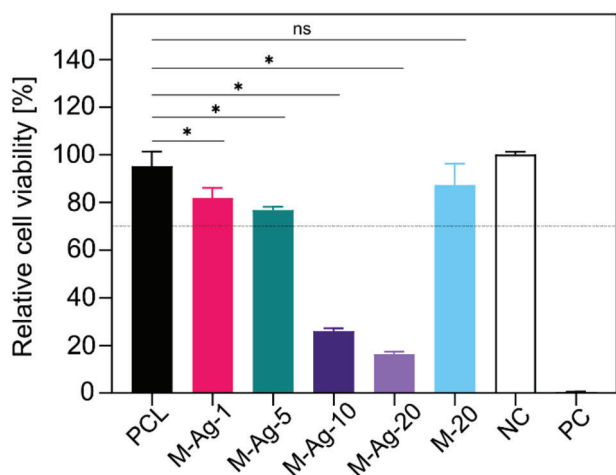


Figure 5. Relative cell viability of smooth muscle cells for the melt-electrowritten scaffolds. Indirect cytocompatibility evaluation of PCL and PCL/MOF–Fe/Ag scaffolds after 72 h cell incubation with the eluates. The absorption is normalized to that of the negative control (NC) and the positive control (PC) is represented. Values represent mean \pm standard deviation obtained from $n = 5$ independent samples.

Another important aspect to investigate is the host immune response to the implanted constructs, which is highly relevant for in situ tissue engineering, as the scaffolds would be first infiltrated by immune cells that then guide the recruitment of other cells to form new autologous tissue. To examine the effect of embedding MOF–Fe and MOF–Fe/Ag in PCL on macrophages, the MEW scaffolds were tested in vitro by measuring the release of proinflammatory (tumor necrosis factor alpha (TNF α), interleukin 6 (IL-6)) and anti-inflammatory cytokines (IL-10, transforming growth factor beta (TGF- β)) after culturing M0 macrophages on the constructs for 72 h. The M–Ag-5 and M-5 scaffolds showed an increase of TNF α and IL-6 cytokines compared to PCL (Figure 7a,b). It is expected that upon implantation, an inflammatory state with proinflammatory cytokine production combined with a macrophage-driven scaffold degradation is induced. The macrophages are hence polarized toward the proinflammatory M1 phenotype.^[84] However, the melt-electrowritten M–Ag-5 scaffolds also showed an increase in the anti-inflammatory cytokines (Figure 7c,d), which would indicate a polarization toward an M2 phenotype, supporting a resolution of the inflammatory phase, and facilitating wound healing and tissue regeneration.^[85–89] The desired host response to foreign bodies includes an inflammatory reaction, and a facilitation of tissue regeneration.^[90,91] Studies examining the cytokine production for pure silver have shown both a release of proinflammatory cytokines, such as TNF α , as well as

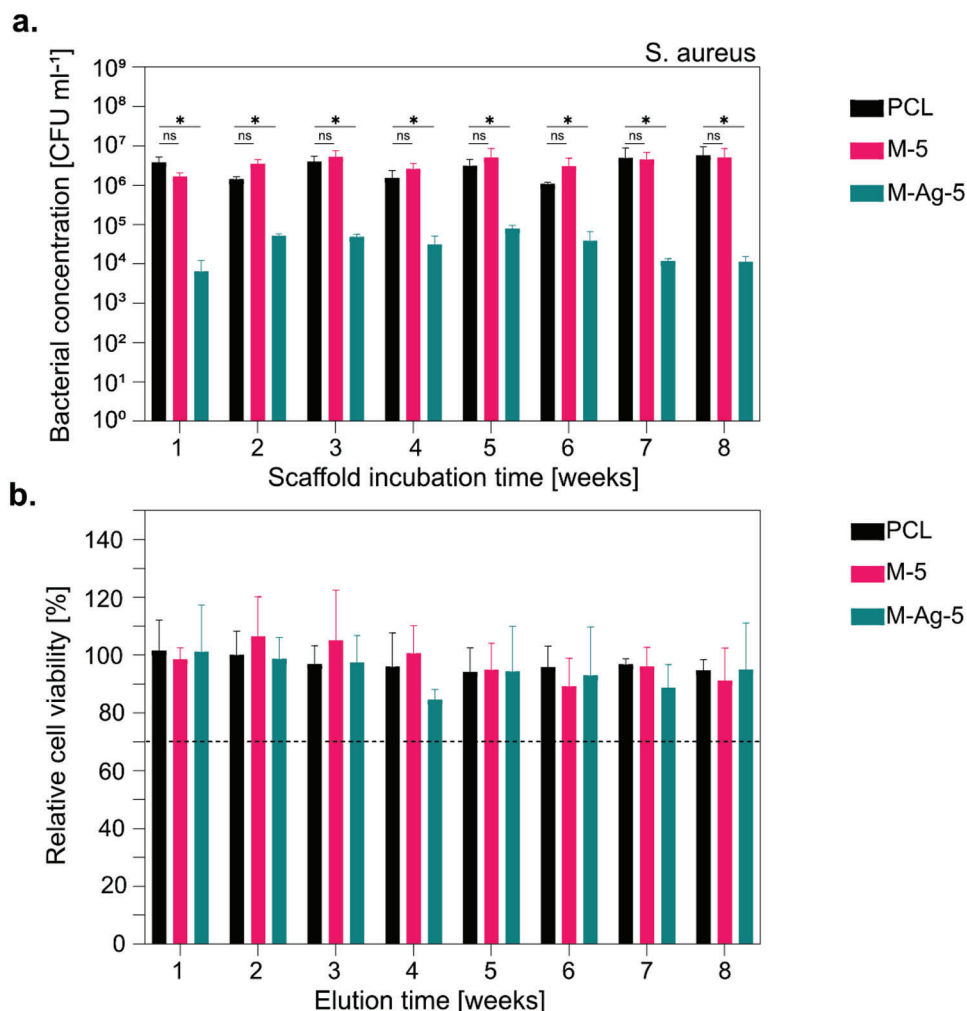


Figure 6. Overview of the antibacterial efficacy and cytotoxicity of the melt-electrowritten PCL, M-5, and M-Ag-5 scaffolds after 1–8 weeks incubation in cell culture medium at 37 °C. a) Bacterial concentration in CFUs is determined for *S. aureus*. Values represent mean \pm standard deviation as obtained from $n = 4$ independent samples. b) Relative cell viability of smooth muscle cells after 72 h exposure to eluates from PCL, M-5, and M-Ag-5 scaffolds over 8 weeks. The absorption is normalized to that of the negative control. Values represent mean \pm standard deviation obtained from $n = 5$ independent samples.

anti-inflammatory cytokines, such as IL-10, to further wound healing and dampen the immune reaction.^[100–103,92–99] The relative ratio of M1 macrophage proinflammatory cytokine release to M2 macrophage anti-inflammatory cytokine release (M1/M2 ratio) showed a slight, although significant, increase for the M-5 and M-Ag-5 scaffolds in comparison to PCL (Figure 7e). However, the ratios are smaller than 1, indicating that the composite scaffolds would maintain a similar response as the widely used PCL.

Finally, we investigated the MRI visibility of the MEW scaffolds (Figure 8a). The melt-electrowritten pure PCL scaffolds were only slightly detectable in nominally T1-weighted images and showed no contrast with agar-agar in R1, R2, and R2* relaxation rate maps, which is shown in Figure 8b. This was likely caused by the low proton density of PCL compared to the proton-rich environment of agar-agar, in which the scaffolds were embedded. Poor MR contrast of pure PCL melt-electrowritten scaffolds was previously reported by Mueller et al. and was increased

via incorporation of USPIO nanoparticles that functioned as contrast agents, strongly affecting the R2* rates in correlation to the weight fraction of USPIO loading.^[15] Here, the M-5 and M-Ag-5 scaffolds generally showed markedly improved visibility in nominally T1-weighted images. However, those scaffolds showed no effects in R1 (longitudinal) relaxation rate maps as seen with pure PCL. Conversely, when investigating the R2 (transverse) maps, the composite materials improved contrast with agar-agar, clearly resolving the triangular architecture of the scaffolds. In R2* relaxation rate maps, strongly increased R2* rates were observed for M-5 and M-Ag-5 scaffolds. To quantify these findings, the R2* map data were averaged for each scaffold in a region of interest and fitted with an exponential plus constant model. Relative to the pure PCL scaffold, a nearly tenfold increase of the apparent average R2* rate for M-5 and M-Ag-5 scaffolds in agar-agar was observed, as shown in Figure 8c. The lack of contrast in R1 maps was indicative of the fact that the strong contrast changes seen in nominally T1-weighted MR images were

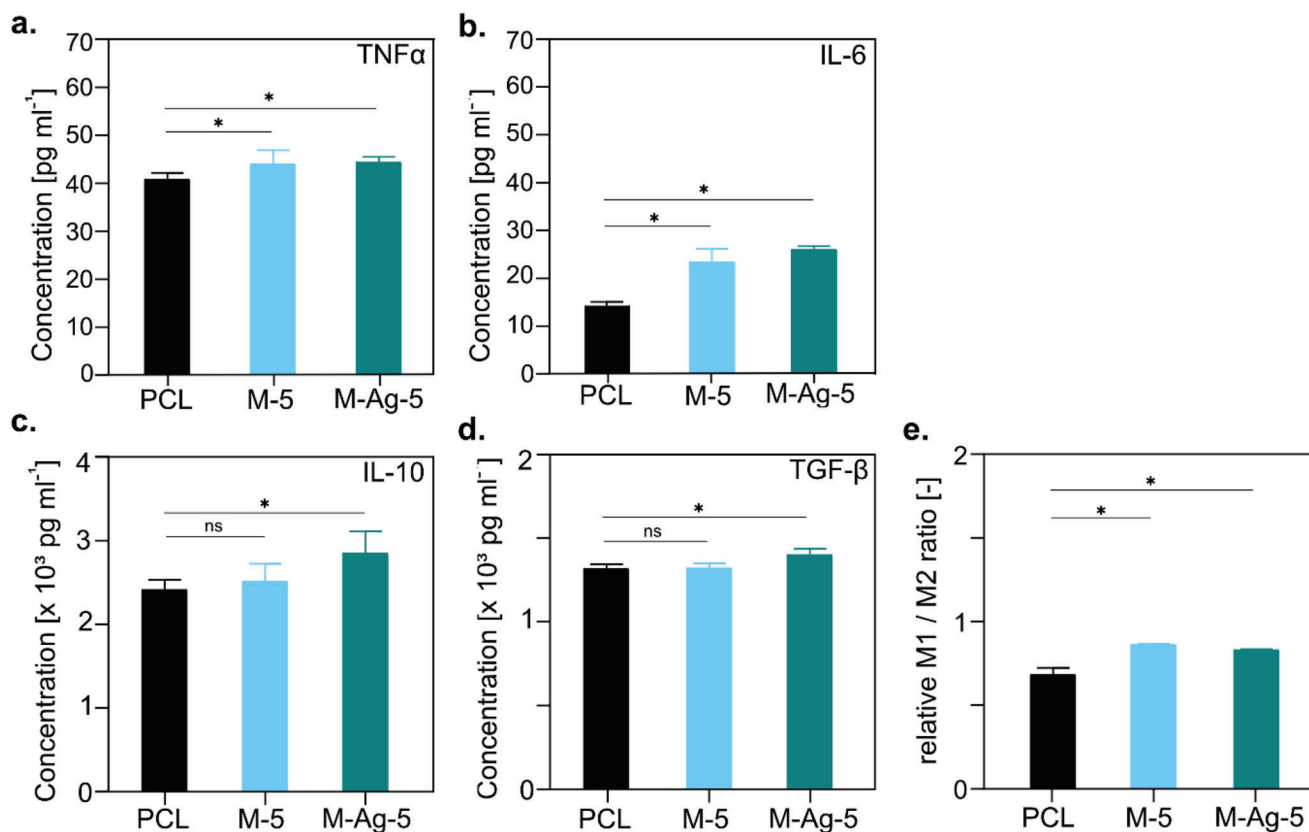


Figure 7. Immune response of M0 monocyte-derived macrophages to the PCL, M-5, and M-Ag-5 scaffolds. Concentration of the cytokines: a) TNF α , b) IL-6, c) IL-10, and d) TGF- β after the incubation of the M0 macrophages on the melt-electrowritten constructs for 72 h, in comparison to pure PCL melt-electrowritten scaffolds. e) Relative M1/M2 ratio of the melt-electrowritten scaffolds. Values represent mean \pm standard deviation as obtained from $n = 4$ independent scaffolds.

caused by the large effects on the $R2^*$ relaxation rate. MOFs acted as negative contrast agents, as they effectively resulted in locally darkened MR images^[104] and therefore significantly improved contrast with the surrounding agar-agar. These findings are in agreement with previous studies, that applied MOF particles for MRI visibility.^[28–30,33] The difference in the $R2^*$ rate for M-5 and M-Ag-5 scaffolds could be contributed to the interference of the silver species. MRI is a clinically accepted non-invasive imaging method that allows both the monitoring of implants as well as the diagnosis and targeted therapy of diseased tissue, e.g., by enabling enhanced visualization of tumors and by delivering drugs loaded into the MOF pores directly in the vicinity of tumors.^[105,106,28–32,35] For example, MIL-88B also features a “breathing effect” which means that the framework’s unit cell is capable of reversibly swelling and shrinking under the influence of an external stimulus without alteration or disruption of the network topology. Leveraging this behavior, governed by host–guest interactions, makes MIL-88B a candidate for controlled drug loading/delivery systems.^[60,61,107] Exploiting this “gate-closing” function, a drug can be loaded in organic solvents and only slowly released through disintegration of the framework under physiological conditions.

A recently published study showed the drug loading of the MIL-88B powder with 5-fluorouracil (FU) to obtain a

delivery system for the cytostatic anticancer drug.^[108] Therefore, to further highlight the versatility of MOFs to obtain multifunctional materials, we proceeded with a proof-of-concept drug-loading and release experiment with FU as model drug.

Here, the silver-decorated MOF (NH_2 -MIL88B-(Fe/Ag)) was loaded with FU (Figures S20–S24, Supporting Information) to obtain FU@MOF-Fe/Ag, according to the recently published study,^[108] PCL/FU@MOF-Fe/Ag scaffolds were produced by MEW, and the release of the drug from the scaffolds was quantified (Figure S25, Supporting Information). While serving as promising preliminary results for follow-up studies, these findings prove that multiple sequential loadings can be performed and, more relevant to our final goal, that MOFs are highly suited to design advanced multifunctional materials for a wide range of biomedical applications. Future studies will investigate the release kinetics from drug-loaded MOFs within the polymer matrix to better understand the mechanism and tune the release.

3. Conclusion

This study presents the first approach for creating multifunctional tissue engineering scaffolds by combining MEW with MOFs. The melt-electrowritten antibacterial, MRI-visible

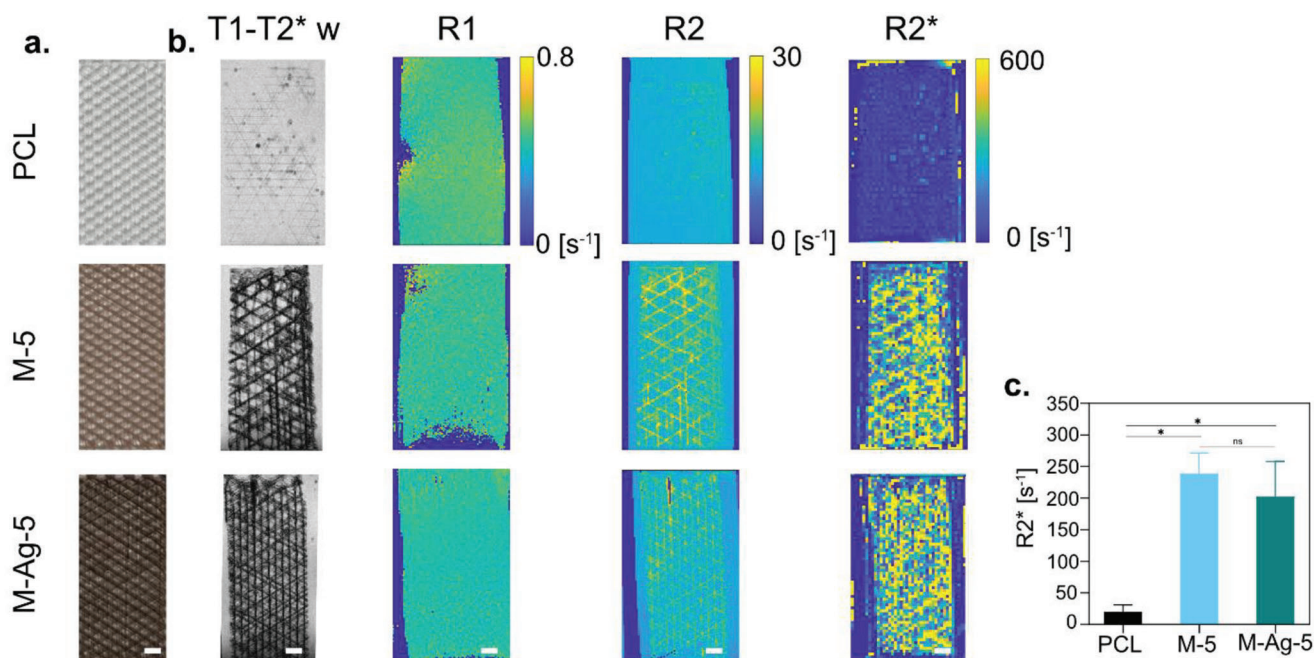


Figure 8. Photographs and MR images of the PCL, M-5, and M-Ag-5 scaffolds. a) Macroscopic images of the melt-electrowritten scaffolds. b) Nominally T1-weighted (and also slightly T2* weighted) MRI of the scaffolds embedded in agar-agar, and the R1, R2, and R2* maps of M-5 and M-Ag-5 in comparison to pure PCL (scale bar 1 mm). c) Averaged R2* rates per scaffold ROI. Values represent mean \pm standard deviation as obtained from $n = 3$ independent scaffolds.

scaffolds could potentially contribute to reducing the risk of postoperative infections and enable noninvasively longitudinally monitoring after implantation. Although here demonstrated with these specific properties, MOFs offer unlimited possibilities for functionalization because of their versatility and complex structures. This combined with the unique capability of MEW to create highly controlled, spatially heterogeneous fibrous constructs, can result in scaffolds with region-specific properties. Therefore, with this study, we pave the way for application-tailored multifunctional constructs, which can be employed in different fields.

4. Experimental Section

For the synthesis of the MOFs, 2-aminoterephthalic acid was purchased from Alfa-Aesar. Metal salts and solvents were purchased from Sigma-Aldrich. All chemicals were used directly without any treatment.

Synthesis of NH₂-MIL-88B-(Fe) and NH₂-MIL-88B-(Fe/Ag): Pristine iron-based NH₂-MIL-88B-(Fe) was synthesized solvothermally from iron(III) chloride hexahydrate, 2-aminoterephthalic acid, deionized water as solvent, and acetic acid as a modulator, as previously reported.^[109] Ag species (identified as Ag/AgCl) were loaded onto the MOF via a one-step postsynthesis modification method.^[56] Experimental details and further characterization (PXRD and SEM) (Figures S2–S4) are provided in Supporting Information (sections 2.1–2.2). For simplicity, NH₂-MIL-88B-(Fe) and NH₂-MIL-88B-(Fe/Ag) were referred to as MOF-Fe and MOF-Fe/Ag, respectively.

Material (MOF Powder) Characterization: The PXRD measurements of the as-prepared MOFs were performed with a Rigaku MiniFlex 600-C diffractometer with X-ray Cu K α radiation (1.5406 Å) and using Bragg-Brentano geometry. TGA of MOFs was carried out using Mettler Toledo STARe System TGA/DSC 3+ apparatus under various atmospheres with

a heating ramp of 10 °C min⁻¹ up to 800 or 1000 °C. FTIR was measured with a PerkinElmer Frontier spectrometer. The TEM images were recorded on a Jeol JEM-1400 Plus operated at 120 kV. XPS was performed on a Leybold-Heraeus LHS 10 spectrometer using a nonmonochromatized Al-K α source (1486.7 eV) at constant pass energy of 100 eV. All characterization techniques are described in more detail in the Supporting Information.

Preparation of PCL/MOF Composites: PCL (Purasorb PC 12, Corbion Purac Biochem, Netherlands) was dissolved in chloroform (VWR Deutschland). Subsequently, the MOF-Fe or MOF-Fe/Ag powder at weight percentages: 1, 5, 10, or 20 wt% relative to the polymer weight (wt%) were added to the polymer solution vials and stirred overnight on a magnetic stirrer at 400 rpm. Samples prepared with 1, 5, 10, or 20 wt% of MOF-Fe and MOF-Fe/Ag were referred to as M-1, M-5, M-10, or M-20, and M-Ag-1, M-Ag-5, M-Ag-10, or M-Ag-20, respectively. After complete dissolution of the polymer and dispersion of the MOF, the solutions were dried in a fume hood as sheets followed by further drying in a vacuum oven for 6 h at 500 mbar. The dried sheets were cut in small pieces and loaded in the 3 cc syringes (Nordson Deutschland GmbH) for MEW. The syringe pistons were then inserted behind the polymer sheets and the syringes were heated to 75 °C at 500 mbar to melt the polymer pieces inside. The pistons were pushed up toward the needle side to form a single polymer block without air bubbles. The syringes were then stored at -20 °C until use.

Rheology: All rheological measurements were conducted on a shear rheometer (MCR102, Anton Paar, Graz, Austria) equipped with a planar bottom plate (P-PTD200, Anton Paar) and a planar PP25 (Anton Paar) measuring head. The gap size between the bottom plate and the measuring head was set to 300 μ m for all experiments. For each trial, the solid sample (roughly 300 mg) was placed onto the bottom plate of the rheometer and then liquified for 5 min by adjusting the temperature to 85 °C, which was the needle temperature in the MEW setup. During melting, the measuring head was slowly lowered until the desired gap size was reached and the gap was sufficiently filled with the molten polymer. To quantify the viscoelastic material response, the storage modulus (G') and the loss modulus (G'') were determined for oscillation frequencies ranging from

0.6 to 10 Hz during all measurements. For measurements conducted at 85 °C, the shear strain was set to a constant value of 1.0%. After the performed frequency sweep, the temperature was lowered to 30 °C, which was the temperature of the print bed, and after a waiting time of 5 min, a second trial was started: G' and G'' were again measured for oscillating frequencies ranging from 0.6 to 10 Hz. This time, the shear strain was set to the 1.5-fold value of the averaged shear strain obtained when applying an oscillatory torque of 0.5 μNm . These averaged shear strain values were determined for every sample in a pretest and averaged over 5 recorded data points. This spectrum was chosen to ensure good data validity (for measurements conducted at 30 °C, where the samples were very stiff, data obtained at lower frequencies became very noisy). This procedure was followed to ensure that all measurements were conducted in the linear regime of the material response. For each measurement representing an individual sample, the moduli measured for different frequencies were averaged.

Melt Electrowriting: Prior to printing, the syringes were equilibrated to room temperature and then inserted in the printhead of the MEW setup.^[9,110] Details to the printer setup are provided in Section S1.9 (Supporting Information). The composites were melted at 75 °C in the syringe and at 85 °C at the 23 G needle (Nordson Deutschland GmbH), through which they were extruded onto a grounded flat metal print bed. Pressurized air was applied to the cartridge and a voltage was applied to the needle. The pressure, voltage, and the speed between the needle and the collector, were determined for the composites, as listed in Table 1. The distance between needle tip and the glass slides placed on the collector was set at 5 mm. For the determination of the fiber diameter and the mapping of the MOF distribution, square patterns with an interfiber distance of 800 μm and a total of 8 layers were melt-electrowritten. For the biological testing and MRI, a triangular pattern with 60°, a distance of 600 μm between parallel fibers, and a total of 8 layers were melt-electrowritten.

Scanning Electron Microscopy: The morphology of the fibrous scaffolds was characterized by scanning electron microscopy (JEOL-JSM-6390, Jeol, Echting, Germany). Prior to the imaging, the scaffolds were left overnight in a vacuum desiccator and then coated with a gold layer using a sputter coater (BAL-TEC, SCD 005, Balzers, Liechtenstein) in saturated argon gas. The scaffolds were imaged at a working distance of 12 mm, and an accelerating voltage of 10 kV. The diameter of the fibers was determined by measuring 20 fibers on different scaffolds ($n = 3$) with the built-in software of the microscope. The MOF—Fe/Ag distribution in the melt-electrowritten constructs was recorded by JEOL JSM-7500F (high resolution) field emission scanning electron microscope through the EDX mapping. For the elemental mapping of the composite melt-electrowritten structures, EDX INCA System (software) with 50 mm^2 X-MAX detector from Oxford Instruments was employed.

Antibacterial Test: The antibacterial efficacy of the melt-electrowritten constructs was evaluated for the strains *S. epidermidis* American type culture collection (ATCC) 14990, *S. aureus* national collection of type cultures (NCTC) 8325-4, and *E. coli* ATCC 25922. The scaffolds were sterilized by washing in 70% ethanol for 2 h and subsequently rinsed 3 times with sterile PBS. The bacterial strains frozen in cryovials were reconstituted with sterile PBS. The bacterial suspensions were then inoculated at a concentration of 10^7 CFU mL^{-1} onto the sterilized scaffolds. After an incubation time of 3 h at 37 °C, these scaffolds were subsequently transferred into Eppendorf tubes and vortexed in sterile PBS for 1 min to detach the adherent bacteria from the scaffold surface. The bacterial suspension for each scaffold was then serially diluted and plated onto Chapman Agar (Sigma, Darmstadt, Germany) in duplicates using the automatic dilutor and plater easySpiral Dilute (Interscience, France). The agar plates were incubated at 37 °C for 72 h and the colonies were counted using the Scan 500 (Interscience, France) to determine the viable bacteria concentration for each scaffold. Bacterial reduction was determined in comparison to the PCL scaffolds, which functioned as a control.

Indirect Cytocompatibility Test: The cytocompatibility experiments were conducted with smooth muscle cells (SMCs) cultured in Dulbecco's modified Eagle medium (DMEM, Gibco) supplemented with 10% v/v fetal calf serum (FCS, Gibco), and 1% antibiotics/antimycotics (ABM, Gibco) at 37 °C in a humidified atmosphere containing 5% CO_2 . The test was

conducted according to ISO 10993. Briefly, the melt-electrowritten scaffolds were sterilized using two 70% ethanol washing steps for 60 min each and subsequently a rinse step with PBS (Gibco) overnight. To create the eluates, scaffolds were incubated in DMEM for 72 h at 37 °C. The eluate of a latex glove was used as a positive control (PC), and untreated medium was used as a negative control (NC). Prior to the eluate transfer, the SMCs were cultured in untreated medium in 96 wells at a density of 10 000 cells cm^{-2} for 24 h. Subsequently, the cells were washed with PBS and the eluates were then transferred onto the SMCs seeded in the 96 wells. The cells were incubated for 3 days at 37 °C and 5% CO_2 . Cell viability was determined for five replicates per scaffold material composition at day 3 using a commercial proliferation test kit (2,3-bis-(2-methoxy-4-nitro-5-sulphophenyl)-2H-tetrazolium-5-carboxanilide, XTT, Invitrogen) following the manufacturer's instructions. The optical density was measured at 450 nm on a microplate reader (Spark, Tecan). The relative absorbance was determined by normalizing the absorbance values to that of the negative control.

Long-Term Indirect Cytocompatibility Test: The long-term indirect cytocompatibility experiment was conducted over eight weeks with SMCs cultured in DMEM (Gibco) supplemented with 10% v/v FCS (Gibco), and 1% ABM (Gibco) at 37 °C in a humidified atmosphere containing 5% CO_2 . Briefly, the melt-electrowritten scaffolds were sterilized twice with 70% ethanol for 60 min and subsequently washed with PBS (Gibco) overnight. To create the eluates, scaffolds were incubated in DMEM for up to eight weeks at 37 °C. The eluate of a latex glove served as the PC, and untreated medium as the NC. At the end of each week during the eight-week incubation period, the scaffolds at T1 to T8 were extracted at the corresponding time points and the eluates stored at 4 °C. After the end of the eight-week incubation period, the SMCs were cultured in untreated medium in 96 wells at a density of 10 000 cells cm^{-2} for 24 h. Then, the cells were washed with PBS and the eluates were then transferred onto the SMCs in the 96 wells. After an incubation time of 3 days at 37 °C and 5% CO_2 , the cell viability was determined using a commercial proliferation test kit (XTT, Invitrogen) following the manufacturer's instructions for five replicates per material composition. The optical density was measured at 450 nm on a microplate reader (Spark, Tecan). The relative absorbance was determined by normalizing the absorbance values to that of the negative control.

Long-Term Antibacterial Test: The antibacterial efficacy of the melt-electrowritten constructs after an incubation period of 1–8 weeks in DMEM (Gibco) at 37 °C was evaluated for *S. aureus* NCTC 8325-4. At the end of each week during the eight-week incubation period, the scaffolds at T1 to T8 were extracted at the corresponding time points and stored at -20 °C. The scaffolds were sterilized in 70% ethanol for 2 h. Then, they were rinsed 3 times with sterile PBS. The frozen bacterial suspension was reconstituted with sterile PBS to a concentration of 10^7 CFU mL^{-1} . After inoculation, the scaffolds were incubated for 3 h at 37 °C. Subsequently, they were transferred into Eppendorf tubes and vortexed in sterile PBS for 1 min to detach the adherent bacteria from the surface. To quantify the viable bacterial concentration, the detached bacterial suspension for each scaffold was serially diluted and plated onto Chapman Agar (Sigma, Darmstadt, Germany) in duplicates using the automatic dilutor easySpiral Dilute (Interscience, France). After incubation for 72 h at 37 °C, the colonies were counted using the Scan 500 (Interscience, France). Bacterial reduction was determined in comparison to the PCL scaffolds, which functioned as a control.

In Vitro Pro-/Anti-Inflammatory Cytokine Release: The immune response to the scaffolds was evaluated by the cytokine expression of monocyte-derived macrophages. For this test, human cell line U937 (ATCC) were cultured in Roswell Park Memorial Institute (RPMI) 1640 medium (Gibco, Life Technologies, UK) supplemented with 10% v/v fetal calf serum (Gibco, Life Technologies, UK), L-glutamine (2 mM, Gibco, Life Technologies, UK), sodium pyruvate (1 mM, Gibco, Life Technologies, USA), penicillin (1 U mL^{-1} , Gibco, Life Technologies, USA), and streptomycin (1 $\mu\text{g mL}^{-1}$, Gibco, Life Technologies, USA). The cells were then differentiated into M0 macrophages using phorbol 12-myristate 13-acetate (100 nM, Sigma-Aldrich) for 72 h and rested in complete culture medium for 24 h before the assay. The monocyte-derived macrophages M0 were seeded at a density of 900 000 cells cm^{-2} on the

scaffolds and the cytokine concentration in the cell culture supernatant was evaluated at 72 h. The determination of the released proinflammatory (IL-6 and TNF α) and anti-inflammatory (TGF- β and IL-10) cytokines was performed with the DuoSet enzyme-linked immunosorbent assay (ELISA) kits for TGF- β , IL-6, IL-10, and TNF α (R&D Systems, Minneapolis, MN, USA) following the manufacturer's instructions using a Multimode Microplate Reader (Tecan, Spark). The M1/M2 index was calculated as previously described in literature.^[90,111,112] Briefly, for each cytokine, the average production was determined over this cytokine's sum production for all melt-electrowritten scaffolds. Then, the percentage of each scaffold's cytokine production was calculated in relation to the aforementioned average. The relative M1/M2 index was then calculated by dividing the average of the M1 cytokines (TNF α , IL-6) by the average of the M2 cytokines (IL-10, TGF- β) per scaffold.

Magnetic Resonance Imaging: MR images of agar-agar-embedded scaffolds in glass tubes were acquired on 7 T preclinical scanner (Agilent Discovery MR901 magnet and gradient system, Bruker AVANCE III HD electronics) with a 10 mm inner diameter proton-tuned solenoid coil (RAPID Biomedical) for radiofrequency transmission and signal reception. Tubes were fixed in place with adhesive tape to avoid motion during imaging due to gradient-induced vibrations and were at lab temperature of $\approx 18^\circ\text{C}$, which was not otherwise controlled. Images were acquired with excitation slices aligned manually to the approximate planes of the embedded scaffolds, as seen in initial scout images. To resolve the details of the scaffolds, T1-weighted (T1w) spoiled gradient recalled echo fast low-angle shot (FLASH) images were acquired with slice thickness 0.5 mm, field of view (FOV) $16 \times 10 \text{ mm}^2$ fully sampled k -space acquisition and reconstruction matrix size 256×160 , repetition time 150 ms, echo time 3 ms, and excitation flip angle 10° . Relaxation rate mapping was acquired with the same slice orientation and thickness and FOV as the T1w images. R1 maps were acquired with a nonselective adiabatic inversion-recovery rapid acquisition with relaxation enhancement (RARE) sequence with inversion times between 80 and 5000 ms, recovery time 2000 ms, echo time 7.6 ms, RARE-factor 4, acquisition matrix 128×80 , and no averaging. R2 maps were acquired with a multi-echo-time RARE sequence with repetition time 2000 ms, echo times between 8 and 64 ms, RARE factor 1, acquisition matrix 128×80 , and 4 averages. R2* maps were acquired with a multigradient recalled echo sequence with repetition time 600 ms, echo times between 1.75 and 18.1 ms, 1.09 ms echo spacing, 16 echoes per excitation with flyback same-direction readout, acquisition matrix 64×40 , and 12 averages. Relaxation rate maps were fit in MatLab 2020a (The MathWorks) with custom-written scripts. Two-parameter exponential decay (R2) or three-parameter exponential plus constant (R1 and R2*) models were least-squares fit for each voxel. For R2*, regions of interest were drawn on the images and the signals averaged before fitting, giving a region-of-interest (ROI)-average fit R2* for each scaffold.

Statistical Analysis: The results are expressed as the mean \pm standard deviation. The Shapiro Wilk test and Lilliefors test were applied to test for the normal distribution of the samples, and a two-sample F -test was employed to check for equal variances. The statistical analysis was performed with an unpaired two-sided t -test between the groups with normal distribution conducted, when homogeneity of variances was met, and for sample groups with unequal variances, the unpaired two-sided t -test with Welch's correction was applied. For sample groups with no normal distribution, the Mann-Whitney test was applied. Statistically significant level was determined at $p < 0.05$. All the data were analyzed using GraphPad Prism 9 and Matlab (version R2019a, MathWorks, Natick, MA, USA).

Supporting Information

Supporting Information is available from the Wiley Online Library or from the author.

Acknowledgements

The authors are grateful to Christine Benning for the ICP-MS measurements. Support from TUM Innovation network project ARTEMIS and from

the German Research Foundation (DFG – Project numbers: 403170227 Ar-chiTissue and 316376997 COORNETS) is acknowledged.

Open access funding enabled and organized by Projekt DEAL.

Conflict of Interest

The authors declare no conflict of interest.

Data Availability Statement

The data that support the findings of this study are available from the corresponding author upon reasonable request.

Keywords

antibacterial, magnetic resonance imaging, melt electrowriting, metal-organic frameworks, polycaprolactone, tissue engineering scaffolds

Received: May 4, 2023

Revised: August 27, 2023

Published online: September 26, 2023

- [1] S. J. Hollister, *Adv. Mater.* **2009**, *21*, 3330.
- [2] M. Castilho, A. van Mil, M. Maher, C. H. G. Metz, G. Hochleitner, J. Groll, P. A. Doevandans, K. Ito, J. P. G. Sluijter, J. Malda, *Adv. Funct. Mater.* **2018**, *28*, 1803151.
- [3] T. D. Brown, P. D. Dalton, D. W. Hutmacher, *Adv. Mater.* **2011**, *23*, 5651.
- [4] G. Hochleitner, T. Jüngst, T. D. Brown, K. Hahn, C. Moseke, F. Jakob, P. D. Dalton, J. Groll, *Biofabrication* **2015**, *7*, 035002.
- [5] A. Hrynevich, B. S. Elçi, J. N. Haigh, R. McMaster, A. Youssef, C. Blum, T. Blunk, G. Hochleitner, J. Groll, P. D. Dalton, *Small* **2018**, *14*, e1800232.
- [6] M. L. Muerza-Cascante, D. Haylock, D. W. Hutmacher, P. D. Dalton, *Tissue Eng., Part B* **2015**, *21*, 187.
- [7] O. Bas, E. M. De-Juan-Pardo, C. Meinert, D. D'angella, J. G. Baldwin, L. J. Bray, R. M. Wellard, S. Kollmannsberger, E. Rank, C. Werner, T. J. Klein, I. Catelas, D. W. Hutmacher, *Biofabrication* **2017**, *9*, 025014.
- [8] E. Hewitt, S. Mros, M. McConnell, J. D. Cabral, A. Ali, *Biomed. Mater.* **2019**, *14*, 55013.
- [9] N. T. Saidy, F. Wolf, O. Bas, H. Keijdener, D. W. Hutmacher, P. Mela, E. M. De-Juan-Pardo, *Small* **2019**, *15*, e1900873.
- [10] T. Jungst, I. Pennings, M. Schmitz, A. J. W. P. Rosenberg, J. Groll, D. Gawlitza, *Adv. Funct. Mater.* **2019**, *29*, 1905987.
- [11] N. T. Saidy, T. Shabab, O. Bas, D. M. Rojas-González, M. Menne, T. Henry, D. W. Hutmacher, P. Mela, E. M. De-Juan-Pardo, *Front. Bioeng. Biotechnol.* **2020**, *8*, 793.
- [12] J. C. Kade, P. D. Dalton, *Adv. Healthcare Mater.* **2021**, *10*, e2001232.
- [13] J. C. Kade, E. Bakirci, B. Tandon, D. Gorgol, M. Mrlik, R. Luxenhofer, P. D. Dalton, *Macromol. Mater. Eng.* **2022**, *307*, 2200478.
- [14] K. Somszor, O. Bas, F. Karimi, T. Shabab, N. T. Saidy, A. J. O'connor, A. V. Ellis, D. Hutmacher, D. E. Heath, *ACS Macro Lett.* **2020**, *9*, 1732.
- [15] K. M. A. Mueller, G. J. Topping, S. P. Schwaminger, Y. Zou, D. M. Rojas-González, E. M. De-Juan-Pardo, S. Berensmeier, F. Schilling, P. Mela, *Biomater. Sci.* **2021**, *9*, 4607.
- [16] N. C. Paxton, J. Ren, M. J. Ainsworth, A. K. Solanki, J. R. Jones, M. C. Allenby, M. M. Stevens, M. A. Woodruff, *Macromol. Rapid Commun.* **2019**, *40*, e1900019.
- [17] A. Abdal-Hay, N. Abbasi, M. Gwiazda, S. Hamlet, S. Ivanovski, *Eur. Polym. J.* **2018**, *105*, 257.

- [18] G. Hochleitner, M. Kessler, M. Schmitz, A. R. Boccaccini, J. Teßmar, J. Groll, *Mater. Lett.* **2017**, *205*, 257.
- [19] Z. Meng, J. He, Z. Xia, D. Li, *Mater. Lett.* **2020**, *278*, 128440.
- [20] M. Yoshida, P. R. Turner, M. A. Ali, J. D. Cabral, *ACS Appl. Bio Mater.* **2021**, *4*, 1319.
- [21] L. Pang, N. C. Paxton, J. Ren, F. Liu, H. Zhan, M. A. Woodruff, A. Bo, Y. Gu, *ACS Appl. Mater. Interfaces* **2020**, *12*, 47993.
- [22] L. Du, L. Yang, B. Xu, L. Nie, H. Lu, J. Wu, H. Xu, Y. Lou, *New J. Chem.* **2022**, *46*, 13565.
- [23] H. Li, M. Eddaoudi, M. O'keeffe, O. M. Yaghi, *Nature* **1999**, *402*, 276.
- [24] O. M. Yaghi, M. O'keeffe, N. W. Ockwig, H. K. Chae, M. Eddaoudi, J. Kim, *Nature* **2003**, *423*, 691.
- [25] S. Hermes, M.-K. Schröter, R. Schmid, L. Khodeir, M. Muhler, A. Tissler, R. W. Fischer, R. A. Fischer, *Angew. Chem., Int. Ed. Engl.* **2005**, *44*, 6237.
- [26] R. J. T. Houk, B. W. Jacobs, F. E. Gabaly, N. N. Chang, A. A. Talin, D. D. Graham, S. D. House, I. M. Robertson, M. D. Allendorf, *Nano Lett.* **2009**, *9*, 3413.
- [27] M. Meilikhov, K. Yusenko, D. Esken, S. Turner, G. Van Tendeloo, R. A. Fischer, *Eur. J. Inorg. Chem.* **2010**, *2010*, 3683.
- [28] K. Böll, A. Zimpel, O. Dietrich, S. Wuttke, M. Peller, *Adv. Ther.* **2020**, *3*, 1900126.
- [29] L. Qin, Z.-Y. Sun, K. Cheng, S.-W. Liu, J.-X. Pang, L.-M. Xia, W.-H. Chen, Z. Cheng, J.-X. Chen, *ACS Appl. Mater. Interfaces* **2017**, *9*, 41378.
- [30] H. Zhou, M. Qi, J. Shao, X. Li, Z. Zhou, S. Yang, H. Yang, *J. Magn. Magn. Mater.* **2021**, *518*, 167436.
- [31] Y. Chen, Z.-H. Li, P. Pan, J.-J. Hu, S.-X. Cheng, X.-Z. Zhang, *Adv. Mater.* **2020**, *32*, 2001452.
- [32] J. Bao, X. Zu, X. Wang, J. Li, D. Fan, Y. Shi, Q. Xia, J. Cheng, *Int. J. Nanomed.* **2020**, *15*, 7687.
- [33] H. Bunzen, D. Jiráč, *ACS Appl. Mater. Interfaces* **2022**, *14*, 50445.
- [34] J. Yang, Y.-W. Yang, *Small* **2020**, *16*, e1906846.
- [35] H. Zhang, Y. Shang, Y.-H. Li, S.-K. Sun, X.-B. Yin, *ACS Appl. Mater. Interfaces* **2019**, *11*, 1886.
- [36] W. Zhang, X. Ren, S. Shi, M. Li, L. Liu, X. Han, W. Zhu, T. Yue, J. Sun, *J. Wang, Nanoscale* **2020**, *12*, 16330.
- [37] X. Huang, S. Yu, W. Lin, X. Yao, M. Zhang, Q. He, F. Fu, H. Zhu, J. Chen, *J. Solid State Chem.* **2021**, *302*, 122442.
- [38] Y.-M. Wu, P.-C. Zhao, B. Jia, Z. Li, S. Yuan, C.-H. Li, *New J. Chem.* **2022**, *46*, 5922.
- [39] G. Ximing, G. Bin, W. Yuanlin, G. Shuanghong, *Mater. Sci. Eng., C* **2017**, *80*, 698.
- [40] S. Lin, X. Liu, L. Tan, Z. Cui, X. Yang, K. W. K. Yeung, H. Pan, S. Wu, *ACS Appl. Mater. Interfaces* **2017**, *9*, 19248.
- [41] P. Horcajada, R. Gref, T. Baati, P. K. Allan, G. Maurin, P. Couvreur, G. Férey, R. E. Morris, C. Serre, *Chem. Rev.* **2012**, *112*, 1232.
- [42] X. Ma, M. Lepoitevin, C. Serre, *Mater. Chem. Front.* **2021**, *5*, 5573.
- [43] C. Duan, J. Meng, X. Wang, X. Meng, X. Sun, Y. Xu, W. Zhao, Y. Ni, *Carbohydr. Polym.* **2018**, *193*, 82.
- [44] X. Yang, H. Chai, L. Guo, Y. Jiang, L. Xu, W. Huang, Y. Shen, L. Yu, Y. Liu, J. Liu, *Colloids Surf., B* **2021**, *205*, 111920.
- [45] M. Nazari, M. Rubio-Martinez, G. Tobias, J. P. Barrio, R. Babarao, F. Nazari, K. Konstas, B. W. Muir, S. F. Collins, A. J. Hill, M. C. Duke, M. R. Hill, *Adv. Funct. Mater.* **2016**, *26*, 3244.
- [46] M. Pejman, M. D. Firouzjafari, S. A. Aktij, P. Das, E. Zolghadr, H. Jafarian, A. A. Shamsabadi, M. Elliott, M. R. Esfahani, M. Sangermano, M. Sadrzadeh, E. K. Wujcik, A. Rahimpour, A. Tiraferri, *J. Membr. Sci.* **2020**, *611*, 118352.
- [47] J. Quirós, K. Boltes, S. Aguado, R. G. de Villoria, J. J. Vilatela, R. Rosal, *Chem. Eng. J.* **2015**, *262*, 189.
- [48] X. Zhang, Y. Wang, J. Liu, J. Shi, D. Mao, A. C. Midgley, X. Leng, D. Kong, Z. Wang, B. Liu, S. Wang, *Chem. Eng. J.* **2021**, *421*, 129577.
- [49] S. Zhang, J. Ye, Y. Sun, J. Kang, J. Liu, Y. Wang, Y. Li, L. Zhang, G. Ning, *Chem. Eng. J.* **2020**, *390*, 124523.
- [50] M. V. D. Z. Park, A. M. Neigh, J. P. Vermeulen, L. J. J. de la Fonteyne, H. W. Verharen, J. J. Briedé, H. van Loveren, W. H. de Jong, *Biomaterials* **2011**, *32*, 9810.
- [51] E. Fortunati, F. D'angelo, S. Martino, A. Orlacchio, J. M. Kenny, I. Armentano, *Carbon* **2011**, *49*, 2370.
- [52] S. Kumar, S. Raj, S. Jain, K. Chatterjee, *Mater. Des.* **2016**, *108*, 319.
- [53] T. Baati, L. Njim, F. Neffati, A. Kerkeni, M. Bouttemi, R. Gref, M. F. Najjar, A. Zakhama, P. Couvreur, C. Serre, P. Horcajada, *Chem. Sci.* **2013**, *4*, 1597.
- [54] M. T. Simon-Yarza, T. Baati, A. Paci, L. L. Lesueur, A. Seck, M. Chiper, R. Gref, C. Serre, P. Couvreur, P. Horcajada, *J. Mater. Chem. B* **2016**, *4*, 585.
- [55] P. Horcajada, T. Chalati, C. Serre, B. Gillet, C. Sebrie, T. Baati, J. F. Eubank, D. Heurtaux, P. Clayette, C. Kreuz, J.-S. Chang, Y. K. Hwang, V. Marsaud, P.-N. Bories, L. Cynober, S. Gil, G. Férey, P. Couvreur, R. Gref, *Nat. Mater.* **2010**, *9*, 172.
- [56] M. Bao, Y. Liu, X. Sun, J. Ren, Z. Zhang, J. Ke, L. Zeng, *J. Alloys Compd.* **2021**, *862*, 158195.
- [57] S. Bauer, C. Serre, T. Devic, P. Horcajada, J. Marrot, G. Férey, N. Stock, *Inorg. Chem.* **2008**, *47*, 7568.
- [58] Y. Meng, *Nanomaterials* **2015**, *5*, 1124.
- [59] J. W. Han, S. Gurunathan, J.-K. Jeong, Y.-J. Choi, D.-N. Kwon, J.-K. Park, J.-H. Kim, *Nanoscale Res. Lett.* **2014**, *9*, 459.
- [60] C. Serre, S. Bourrelly, A. Vimont, N. A. Ramsahye, G. Maurin, P. L. Llewellyn, M. Daturi, Y. Filinchuk, O. Leynaud, P. Barnes, G. Férey, *Adv. Mater.* **2007**, *19*, 2246.
- [61] M. Ma, A. Bétard, I. Weber, N. S. Al-Hokbany, R. A. Fischer, N. Metzler-Nolte, *Cryst. Growth Des.* **2013**, *13*, 2286.
- [62] E. Bakirci, A. Frank, S. Gumbel, P. F. Otto, E. Fürsattel, I. Tessmer, H.-W. Schmidt, P. D. Dalton, *Macromol. Chem. Phys.* **2021**, *222*, 2100259.
- [63] M. P. Abuçafy, B. L. Caetano, B. G. Chiari-Andréo, B. Fonseca-Santos, A. M. Do Santos, M. Chorilli, L. A. Chiavacci, *Eur. J. Pharm. Biopharm.* **2018**, *127*, 112.
- [64] S.-N. Kim, C. G. Park, B. K. Huh, S. H. Lee, C. H. Min, Y. Y. Lee, Y. K. Kim, K. H. Park, Y. B. Choy, *Acta Biomater.* **2018**, *79*, 344.
- [65] K. A. Mocniak, I. Kubajewska, D. E. M. Spillane, G. R. Williams, R. E. Morris, *RSC Adv.* **2015**, *5*, 83648.
- [66] N. Kaur, P. Tiwari, K. S. Kapoor, A. K. Saini, V. Sharma, S. M. Mobin, *CrystEngComm* **2020**, *22*, 7513.
- [67] S. Anees Ahmad, S. Sachi Das, A. Khatoon, M. Tahir Ansari, M. Afzal, M. Saquib Hasnain, A. Kumar Nayak, *Mater. Sci. Energy Technol.* **2020**, *3*, 756.
- [68] S. Tang, J. Zheng, *Adv. Healthcare Mater.* **2018**, *7*, e1701503.
- [69] W. K. Jung, H. C. Koo, K. W. Kim, S. Shin, S. H. Kim, Y. H. Park, *Appl. Environ. Microbiol.* **2008**, *74*, 2171.
- [70] E. Pazos-Ortiz, J. H. Roque-Ruiz, E. A. Hinojos-Márquez, J. López-Esparza, A. Donohué-Cornejo, J. C. Cuevas-González, L. F. Espinosa-Cristóbal, S. Y. Reyes-López, *J. Nanomater.* **2017**, *2017*, 4752314.
- [71] J. López-Esparza, L. F. Espinosa-Cristóbal, A. Donohue-Cornejo, S. Y. Reyes-López, *Ind. Eng. Chem. Res.* **2016**, *55*, 12532.
- [72] C. A. Dos Santos, M. M. Seckler, A. P. Ingle, I. Gupta, S. Galdiero, M. Galdiero, A. Gade, M. Rai, *J. Pharm. Sci.* **2014**, *103*, 1931.
- [73] W.-R. Li, T.-L. Sun, S.-L. Zhou, Y.-K. Ma, Q.-S. Shi, X.-B. Xie, X.-M. Huang, *Int. Biodeterior. Biodegrad.* **2017**, *123*, 304.
- [74] T. C. Dakal, A. Kumar, R. S. Majumdar, V. Yadav, *Front. Microbiol.* **2016**, *7*, 1831.
- [75] G. Franci, A. Falanga, S. Galdiero, L. Palomba, M. Rai, G. Morelli, M. Galdiero, *Molecules* **2015**, *20*, 8856.
- [76] X. Yan, B. He, L. Liu, G. Qu, J. Shi, L. Hu, G. Jiang, *Metallomics* **2018**, *10*, 557.

- [77] B. Calderón-Jiménez, M. E. Johnson, A. R. Montoro Bustos, K. E. Murphy, M. R. Winchester, J. R. Vega Baudrit, *Front. Chem.* **2017**, *5*, 6.
- [78] N. Miura, Y. Shinohara, *Biochem. Biophys. Res. Commun.* **2009**, *390*, 733.
- [79] P. V. Asharani, G. Low Kah Mun, M. P. Hande, S. Valiyaveetil, *ACS Nano* **2009**, *3*, 279.
- [80] M. Akter, M. T. Sikder, M. M. Rahman, A. K. M. A. Ullah, K. F. B. Hossain, S. Banik, T. Hosokawa, T. Saito, M. Kurasaki, *J. Adv. Res.* **2018**, *9*, 1.
- [81] A. R. Gliga, S. Skoglund, I. Odnevall Wallinder, B. Fadeel, H. L. Karlsson, *Part. Fibre Toxicol.* **2014**, *11*, 11.
- [82] H. Pham, K. Ramos, A. Sua, J. Acuna, K. Slowinska, T. Nguyen, A. Bui, M. D. R. Weber, F. Tian, *ACS Omega* **2020**, *5*, 3418.
- [83] I. Christodoulou, C. Serre, R. Gref, in *Metal-Organic Frameworks for Biomedical Applications*, (Ed: M. Mozafari), Woodhead Publishing, Cambridge, UK, **2020**, pp. 467.
- [84] T. B. Wissing, V. Bonito, C. V. C. Bouten, A. I. P. M. Smits, *npj Regener. Med.* **2017**, *2*, 18.
- [85] M. S. H. Akash, K. Rehman, S. Chen, *Pharm. Res.* **2013**, *30*, 2951.
- [86] W. K. E. Ip, N. Hoshi, D. S. Shouval, S. Snapper, R. Medzhitov, *Science* **2017**, *356*, 513.
- [87] A. P. Hutchins, D. Diez, D. Miranda-Saavedra, *Briefings Funct. Genomics* **2013**, *12*, 489.
- [88] P. J. Murray, *Proc. Natl. Acad. Sci. USA* **2005**, *102*, 8686.
- [89] J. Banchereau, V. Pascual, A. O'garra, *Nat. Immunol.* **2012**, *13*, 925.
- [90] T. B. Wissing, V. Bonito, E. E. van Haften, M. van Doeselaar, M. M. C. P. Bruggmans, H. M. Janssen, C. V. C. Bouten, A. I. P. M. Smits, *Front. Bioeng. Biotechnol.* **2019**, *7*, 87.
- [91] S. Franz, S. Rammelt, D. Scharnweber, J. C. Simon, *Biomaterials* **2011**, *32*, 6692.
- [92] N. Ninan, N. Goswami, K. Vasilev, *Nanomaterials* **2020**, *10*, 967.
- [93] P. Varela, L. Marlinghaus, S. Sartori, R. Viebahn, J. Salber, G. Ciardelli, *Front. Bioeng. Biotechnol.* **2020**, *8*, 124.
- [94] V. Dennis, Yilma, S. Singh, S. Dixit, *Int. J. Nanomed.* **2013**, *8*, 2421.
- [95] K. K. Y. Wong, S. O. F. Cheung, L. Huang, J. Niu, C. Tao, C.-M. Ho, C.-M. Che, P. K. H. Tam, *ChemMedChem* **2009**, *4*, 1129.
- [96] K. K. Y. Wong, X. Liu, *Med. Chem. Commun.* **2010**, *1*, 125.
- [97] M. Giovanni, J. Yue, L. Zhang, J. Xie, C. N. Ong, D. T. Leong, *J. Hazard. Mater.* **2015**, *297*, 146.
- [98] D.-H. Lim, J. Jang, S. Kim, T. Kang, K. Lee, I.-H. Choi, *Biomaterials* **2012**, *33*, 4690.
- [99] F. Martínez-Gutiérrez, E. P. Thi, J. M. Silverman, C. C. de Oliveira, S. L. Svensson, A. V. Hoek, E. M. Sánchez, N. E. Reiner, E. C. Gaynor, E. L. G. Pryzdial, E. M. Conway, E. Orrantia, F. Ruiz, Y. Av-Gay, H. Bach, *Nanomedicine* **2012**, *8*, 328.
- [100] G. Shi, W. Chen, Y. Zhang, X. Dai, X. Zhang, Z. Wu, *Langmuir* **2019**, *35*, 1837.
- [101] T. Gunasekaran, T. Nigusse, M. D. Dhanaraju, *J. Am. Coll. Clin. Wound Spec.* **2011**, *3*, 82.
- [102] J. Tian, K. K. Y. Wong, C.-M. Ho, C.-N. Lok, W.-Y. Yu, C.-M. Che, J.-F. Chiu, P. K. H. Tam, *ChemMedChem* **2007**, *2*, 129.
- [103] C. You, Q. Li, X. Wang, P. Wu, J. K. Ho, R. Jin, L. Zhang, H. Shao, C. Han, *Sci. Rep.* **2017**, *7*, 10489.
- [104] J. Wahsner, E. M. Gale, A. Rodríguez-Rodríguez, P. Caravan, *Chem. Rev.* **2019**, *119*, 957.
- [105] Z. Zhang, W. Sang, L. Xie, Y. Dai, *Coord. Chem. Rev.* **2019**, *399*, 213022.
- [106] R. A. Hamideh, B. Akbari, P. Fathi, S. K. Misra, A. Sutrisno, F. Lam, D. Pan, *Adv. Healthcare Mater.* **2020**, *9*, e2000136.
- [107] P. Horcajada, F. Salles, S. Wuttke, T. Devic, D. Heurtaux, G. Maurin, A. Vimont, M. Daturi, O. David, E. Magnier, N. Stock, Y. Filinchuk, D. Popov, C. Riekkel, G. Férey, C. Serre, *J. Am. Chem. Soc.* **2011**, *133*, 17839.
- [108] M. U. Akbar, M. Badar, M. Zaheer, *ACS Omega* **2022**, *7*, 32588.
- [109] M.-H. Pham, G.-T. Vuong, A.-T. Vu, T.-O. Do, *Langmuir* **2011**, *27*, 15261.
- [110] K. F. Eichholz, I. Gonçalves, X. Barceló, A. S. Federici, D. A. Hoey, D. J. Kelly, *Addit. Manuf.* **2022**, *58*, 102998.
- [111] N. Grotenhuis, Y. Bayon, J. F. Lange, G. J. V. M. Van Osch, Y. M. Bastiaansen-Jenniskens, *Biochem. Biophys. Res. Commun.* **2013**, *433*, 115.
- [112] T. B. Wissing, E. E. van Haften, S. E. Koch, B. D. Ippel, N. A. Kurniawan, C. V. C. Bouten, A. I. P. M. Smits, *Biomater. Sci.* **2019**, *8*, 132.